Towards more sustainable negative electrodes in Na-ion batteries via nanostructured iron oxide

M. Valvo [a,*], F. Lindgren [a], U. Lafont [b], F. Björefors [a], K. Edström [a]

[a] *Department of Chemistry, Ångström Laboratory, Uppsala University, Box 538, 75121 Uppsala, Sweden*
[b] *Novel Aerospace Materials, Aerospace Engineering, Delft University of Technology, 2629 HS Delft, The Netherlands*

HIGHLIGHTS

- Nanostructured Fe_2O_3 is produced by a simple and novel method at low temperature.
- Iron oxide is here investigated as negative electrode in sodium-ion batteries.
- A detailed comparison with iron oxide cycled in Li half cells has been performed.
- Fe_2O_3 is compatible with use in Na-ion batteries at moderate current densities.

GRAPHICAL ABSTRACT
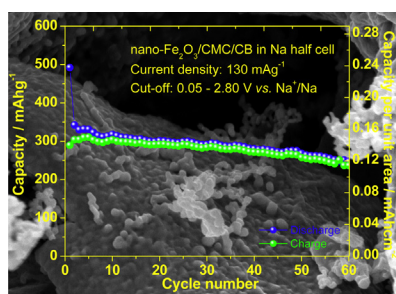
ABSTRACT

Na-ion technology could emerge as an alternative to Li-ion batteries due to limited costs and vast availability of sodium, as well as its similar chemistry. Several Na-rich compounds have been proposed as positive electrodes, whereas suitable negative counterparts have not been found yet. Nanostructured iron oxide is reported here for the first time as a potentially viable negative electrode for Na-ion cells based on conventional electrolytes and composite coatings with carboxymethyl cellulose. Electrochemical reactions of Na^+ and Li^+ ions with nanostructured Fe_2O_3 are analysed and compared. Initial sodiation of Fe_2O_3 yields a sloping profile in a voltage range characteristic for oxide conversion, which instead generates a typical plateau upon lithiation. Application of such earth-abundant, nontoxic material in upcoming Na-ion batteries is potentially groundbreaking, since it offers important advantages, namely: *i.* simple and cost-effective synthesis of Fe_2O_3 nanostructures at low temperatures; *ii.* cheaper and more sustainable cell fabrication with higher energy densities, e.g., use of natural, water-soluble binders, as well as Al for both current collectors; *iii.* electrochemical performances with specific gravimetric capacities exceeding 400 mAh g^{-1} at 40 mA g^{-1}, accompanied by decent specific volumetric energy densities, e.g., ≈ 1.22 Wh cm^{-3}, provided that cycle inefficiencies and long-term durability are addressed.

1. Introduction

Li-ion batteries have received great attention due to their high energy densities, output voltages and versatility, which have made them the main rechargeable power source for portable electronics and, more recently, also for power tools. For these reasons, plug-in electric vehicles (PEVs) and hybrid electric vehicles (HEVs) are soon expected to be powered by advanced Li-ion batteries, which should provide adequate energy and power densities. However, doubts and controversies are raised about the availability of lithium reserves [1], as well as related mining and processing costs to meet the demand of massive production of

* Corresponding author. Tel.: +46 (0)18 4713715; fax: +46 (0)18 513548.
E-mail address: mario.valvo@kemi.uu.se (M. Valvo).

battery modules for EVs [2], unless proper Li recycling is adopted. In this scenario, Na-ion chemistries are considered an attractive alternative, because using sodium instead of lithium would be much cheaper and easier in terms of extraction, processing and recovery. Furthermore, the similarities between Na^+ and Li^+ intercalation reactions favour the use of analogous compounds which could match both applications in this way. However, the specific energy densities of Na-ion battery materials are intrinsically lower than those of Li-ion cells. In fact, the atomic mass of sodium is about three times higher than that of lithium, the Na^+ ion radius is almost one and a half time larger than that of Li^+ and ultimately sodium exhibits a less negative redox potential compared to that of lithium. Although Na-ion battery materials are not comparable with their Li-ion counterparts, there are studies suggesting that Na-ion systems should not be discarded [3] and that under certain conditions they could even try to compete with Li-ion technology [4]. In particular, Na-ion batteries operating at room temperature could be suitable for applications where specific volumetric and gravimetric energy density requirements are not as stringent as in EVs, namely in electrical grid storage of intermittent energy produced via renewable sources, provided that adequate performances and durability are achieved [5]. This would also contribute to a significant reduction of the costs connected to the use of renewable sources, which could then penetrate the energy market more easily and make Na-ion technology complementary to Li-ion batteries for stationary storage. Costs, safety and long-lasting performances are of primary importance in this perspective.

So far, many positive electrodes have been proposed [6–32], whereas only few negative electrode materials have been investigated and even less candidates exist to date as viable anodes for Na-ion batteries. Graphite cannot be used as negative electrode, due to its inability to intercalate Na atoms [33–35]. Metal Na is also ruled out, because, similarly to metallic Li, it forms dendrites and has even a lower melting point than Li, thus raising safety issues. Hard carbons proved to insert and de-insert Na ions, which could adsorb onto the surface of the nano-pores in their structures [34–36], delivering capacities of about 200–300 mAh g^{-1} [36,37]. However, the reversibility for carbonaceous materials still remains a major issue [38]. Moreover, sodiated carbon proved to be more reactive towards non-aqueous electrolytes than its lithiated analogous, causing further instability [39,40]. Recently, tailored carbon nanostructures, e.g., hollow carbon nanowires [41], have been reported to improve both capacity retention and rate capability compared to conventional carbon-based electrodes. Nonetheless, their poor initial coulombic efficiency (i.e. 50.5%) indicates that SEI layer formation and stability towards the electrolyte are not solved by such approach.

Na-alloys have been proposed as a possible alternative, in analogy to Li-alloys, because they could provide higher specific capacities [42]. However, Na-alloys suffer from huge volume changes upon uptake/removal of Na, which are even larger than those for Li-alloys, thus posing greater limitations for the realization of durable electrodes. Na has been reported to cycle reversibly with moderate capacity fading in different hosts such as Sn [43], thin Cu_2Sb films [44] and in Sb/C [45] and SnSb/C [46] nanocomposites for a maximum of 100 cycles with capacities of about 400–600 mAh g^{-1}, necessitating, however, the use of dedicated electrolyte additives (i.e. FEC) [45,47] and/or binders (PAA) [43] to minimise the continuous SEI reconstruction upon expansion/contraction of the alloys. Na alloys would then require, similarly to Li-alloys, special electrode preparations to buffer the volume variations and related cycling issues. Moreover, Na-alloys possess much lower *volumetric* energy densities than Li-alloys [48], due to the larger volume occupied by the Na atoms in the compounds. Both

factors would ultimately spoil the benefits of having low-cost Na raw materials [42].

Transition metal oxides (TMOs) have also been investigated as possible negative electrodes relying on insertion of Na^+ at low voltages. Na_xVO_2 yielded a limited capacity (e.g. <130 mAh g^{-1}) at a C/100 rate and its operation at ≈ 1.5 V vs. Na^+/Na resulted in a low energy density. Moreover, the high sensitivity towards oxygen made such compound not practical [49]. Similarly, insertion/de-insertion of Na^+ in $Na_2Ti_3O_7$ at an average potential of ≈ 0.3 V vs. Na^+/Na exhibited an initial capacity of about 220 mAh g^{-1} which underwent moderate fading at a C/25 rate upon a 5-cycle test [50]. Other TMOs have been suggested for similar purposes, e.g., nanocrystalline Fe_3O_4 and α-Fe_2O_3, whose electrochemical insertion of Li^+ and Na^+ ions was investigated, however, in a potential range mostly suitable for positive electrodes [51]. These oxides exhibited interesting Na^+ insertion/de-insertion for 30 cycles at 20 mA g^{-1} with reversible capacities close to 150 mAh g^{-1} for Fe_3O_4 and to 170 mAh g^{-1} for Fe_2O_3, whereas the application of higher current densities (i.e. 100 mA g^{-1}) caused a significant capacity fading for both. Sodium de-intercalation from layered sodium-iron oxide was also proposed in the 90's as a possible alternative to replace expensive cobalt-based electrodes in secondary batteries [52].

Interstitial-free TMOs can reversibly store large amounts of Li also at low voltages via *conversion* reactions, where the transition metal, M, is displaced and does *not* alloy with lithium, which instead bounds to oxygen according to [53]:

$$M_xO_y + 2yLi^+ + 2ye^- \leftrightarrow xM^0 + yLi_2O \qquad (1)$$
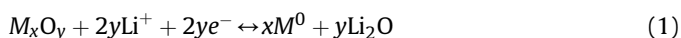
The reduced TMO consequently forms a composite material made of nanosized metallic particles, M^0, dispersed in a surrounding Li_2O matrix. Analogous electrochemical reactions with lithium have also been reported for other transition metal compounds [54–57]. Iron oxides are clearly attractive among convertible TMOs, since they not only exhibit high specific gravimetric and volumetric capacities, but they are also abundant, cheap and nontoxic. They can easily be produced and processed in cost-effective ways, even in various nanostructured forms, with low environmental impact and higher safety compared to most metallic nanostructures, offering compatibility with direct synthesis and incorporation into nanocomposite coated electrodes via single-step approaches [58].

Structural characterization of lithiated iron oxides was initiated in the 80's [59], when it was recognised that "transition metal oxides and sulphides can reversibly accommodate hydrogen or alkali-metal atoms into their structure over a wide range of solid solution" and therefore they were considered "of interest as possible electrodes in secondary batteries" [59,60]. It was also found that electrochemical lithiation at room temperature of both $Li_xFe_3O_4$ and $Li_xFe_2O_3$ first yielded a compositional range of $0 < x < 2$ and subsequently the formation of Li_2O and Fe for $x > 2$, when conversion set in.

Mindful of such key findings, the electrochemical sodiation of nanostructured Fe_2O_3 in composite coated electrodes with Na-carboxymethyl cellulose is investigated here for the first time in a voltage range where not only Na insertion occurs, but also an analogous oxide conversion. This reaction enables access to higher capacities for negative electrodes in Na-ion batteries, while retaining all the advantages of a nanostructured iron-based material as host. The approach and the materials proposed in this study are cost-effective (see Table 1) and enable cycling at current densities as high as 130 mA g^{-1} for more than fifty cycles, displaying a moderate initial columbic loss and capacity fading upon further cycling. Additionally, the synthesis method, as well the binders and

Table 1
Synoptic table of the main properties for the various components commercially utilised (or to be possibly used) in batteries based on Lithium and Sodium ions. Positive electrode materials have not been included for comparison here. Note that the price for Fe_2O_3 is referred to iron ores, whereas its abundance is related to iron in general. The prices for Li and Na are referred to those of lithium carbonate and sodium sulphate, respectively. A very rich variety of other Na sources exists as well.

	Component	Earth abundance (by weight)	Costs (per weight)	ρ (g cm^{-3})	T_m or T_{ev} (°C)	M_{wt} (g mol^{-1})
Main feedstock	Li	18 ppm[b]	5 kUS\$ ton^{-1e}	0.534	180.5	6.941
	Na	22,700 ppm[b]	0.14 kUS\$ ton^{-1e}	0.97	97.8	22.989
Current collectors	Cu	68 ppm[b]	8 kUS\$ ton^{-1d}	8.96	1083.4	63.546
	Al	83,000 ppm[b]	2 kUS\$ ton^{-1d}	2.70	660.3	26.981
Negative active mat.	C[a]	180 ppm[b]	1 kUS\$ ton^{-1e}	2.26	4492	12.011
	Fe_2O_3	62,000 ppm[b]	0.15 kUS\$ ton^{-1e}	5.24	1565	159.69
Polymer binders	PVdF	Synthetic	20 US\$ kg^{-1c}	1.78	170	≈700,000
	CMC	Natural, renewable	6 US\$ kg^{-1c}	1.55	270	≈700,000
Binder solvents	NMP	Synthetic	2–4 US\$ kg^{-1}	1.03	202	99.13
	H_2O	Natural, renewable	<1 US\$ kg^{-1}	1.00	100	18.0

[a] Graphite.
[b] Ref. [94].
[c] Refs. [61,62].
[d] www.indexmundi.com.
[e] http://minerals.usgs.gov/minerals/pubs/commodity.

solvents used for the electrode preparation have limited impact on both environment and health [61,62], making it easier to recycle the materials (e.g. the coatings are water-soluble and eventual calcination of the electrode components does not lead to the formation of obnoxious compounds and gases).

Nonetheless, further efforts are needed to improve the initial reversibility, durability, as well as the round-trip efficiencies for this type of electrodes.

2. Experimental

2.1. Synthesis of nanostructured iron oxide powders

Nanostructured iron oxide powders with a porous texture were synthesised by pyrolysis in vacuum of an iron precursor salt. Anhydrous iron acetate (Aldrich) was loaded into a glass tube in an Ar-filled glove-box (M-Braun) with moisture and oxygen levels below 1 ppm. The tube containing the precursor powder was directly transferred into a tubular furnace (Büchi) connected to a vacuum line without leaving the Ar atmosphere. The precursor was subsequently heated up to 260 °C for 15 h. A colour change was observed for the precursor from the early stages of the thermal treatment. The iron acetate powder progressively changed from bright red to dark brown/black when the temperature approached 200 °C. Full pyrolysis of $Fe(CH_3COO)_2$ and formation of a final nanostructured iron oxide mixture (e.g. γ-Fe_2O_3/α-Fe_2O_3) was therefore obtained without employing any complex procedure. The pyrolysis products, however, were not all immediately known. A number of possible reactions could indeed occur during the pyrolysis in vacuum, being also the solid state mutation of γ-Fe_2O_3 into α-Fe_2O_3 complex in nature [63]. The pyrolytic process induced porosity in the resulting material during the precursor decomposition by releasing gaseous by-products, e.g., carbon dioxide, acetone vapours etc., which were removed by the vacuum. The obtained powders were transferred from the tube to a sealed glass bottle in the glove-box at the end of the thermal treatment.

2.2. Exposure of the nanostructured powders to air

A small amount of the dark brown/black powders was initially taken out from the sealed bottle in the glove-box and exposed to air to check the stability of the products and to carry out preliminary analyses of the material structure and composition. Such powders proved stable in contact with air and did not show any

colour change, retaining their characteristic dark hue. Surprisingly, when the major part of the remaining powders were removed from the glove box and exposed to air to begin with the preparation of electrode coatings, they suddenly began to heat up and release fumes, undergoing a colour change from black to intense red in few minutes.

2.3. Electrode preparation

The reacted powders were used as active material and mixed together with carbon black (CB), e.g., Super P (Timcal Graphite & Carbon) and Na-Carboxymethyl cellulose (CMC − Aldrich, M_w ≈ 700,000, D.S. 0.90) in a weight ratio Fe_2O_3/CMC/CB of 65:15:20. A paste was prepared by adding de-ionised water to the mixed components and by further ball-milling the blend for 1 h. The resulting slurry was casted on a 0.02 mm-thick copper foil by an automatic bar coating equipment (KR − K Control Coater) and dried overnight in a convection oven at 80 °C. Circular coated electrodes with a diameter of 20 mm were cut by a precision perforator (Hohsen) and dried in a tubular vacuum oven (Büchi) to 120 °C for 12 h prior to cell assembly.

2.4. Characterization and electrochemical measurements

The pyrolysed powders were analysed by various microscopy and spectroscopy techniques. X-ray diffraction (XRD) was carried out by a Siemens (D5000) diffractometer with a Cu-K_α radiation source. Scanning Electron Microscopy (SEM) was performed on a Zeiss (Gemini 1550) microscope having a field emission (FE) electron source and an in-lens detector for secondary electrons, coupled with a X-MAX EDX probe (Oxford Instruments) for Energy Dispersive Spectroscopy (EDS) and chemical mapping. Transmission Electron Microscopy (TEM) was carried out using 300 kV-electrons emitted by an electron microscope (FEI Tecnai F20) equipped with a FEG source and a LINK EDX probe (Oxford Instruments) for elemental analysis. The powders were first ground in a mortar and dispersed in absolute ethanol. Few droplets of the resulting suspensions were placed on a carbon-coated copper grid (Quantifoil) to prepare the specimens. Raman micro-spectroscopy was performed at room temperature by a Renishaw RamaScope 2000 equipment having a 50 mW air-cooled laser (Spectra Physics) with a 514 nm excitation wavelength coupled to an optical microscope (Leica) and a Peltier-cooled CCD detector for spectral detection. A notch filter served for removal of Rayleigh scattered light. The laser beam was

focused onto the surface of the samples and its power threshold was maintained at 10 mW, while minimizing beam exposure in-between subsequent scans to prevent possible degradation of the materials. Prior to their analysis, a reference peak at 521 cm^{-1} was obtained for instrument calibration from a (001) Si substrate. The acquisition time for each spectrum was fixed to 15 s and 20 cumulative scans were run to collect the ultimate spectra. The surface area of the powders was characterized by nitrogen phys-isorption measurements, which were carried out at 77 K on a Micromeritics instrument (ASAP 2020) having an ASAP 2020 V3.04 E software. The mixture of reacted γ-Fe$_2$O$_3$/α-Fe$_2$O$_3$ pow-ders was heated overnight at 150 °C before the measurements. Brunauer—Emmett—Teller (BET) method was used to calculate the specific surface area, whereas Barrett—Joyner—Halenda (BJH) calculation was conducted for determining the pore size distribution.

'Coffee-bag' cells were assembled in an Ar-filled glove box (M-Braun) with oxygen and moisture levels below 1 ppm. Different types of batteries were prepared with the same Fe$_2$O$_3$/CMC/CB coating as working electrode, namely: lithium half cells having a metal Li foil as combined reference and counter electrode and so-dium half cells, where metallic Na was utilised in an analogous way. The electrolyte consisted of 1 M LiPF$_6$ in EC:DEC (2:1 by wt.) for the Li half cells, whereas 1 M NaClO$_4$ in EC:DEC (2:1) for the Na half cells. A thin membrane (Solupore) was soaked with the respective electro-lytes and used in the corresponding cells to separate the electrodes.

Cyclic Voltammetry (CV) was performed on a potentiostat/gal-vanostat (VMP2 — Bio-Logic) by applying increasing scan rates between 0.05 and 3.0 V *vs.* Li$^+$/Li or *vs.* Na$^+$/Na for Li- and Na half cells, respectively. Scan rates progressively doubling from 0.1 to 0.8 mV s^{-1} were applied for preliminary electrochemical analysis.

Galvanostatic tests of the respective cells were run on a battery cycler (Digatron — BTS 600) by applying constant current densities between 0.05 and 3.0 V *vs.* Li$^+$/Li or *vs.* Na$^+$/Na. A slightly different cut-off voltage of 0.05 and 2.8 V *vs.* Na$^+$/Na was used as well. The batteries were also discharged and charged using different rates (i.e. applied current densities) to study the rate capability of the electrodes.

3. Results and discussion

3.1. Structural and compositional analysis

This section discusses the structural properties of the resulting materials and compares the characteristic features of the different phases of nanostructured Fe$_2$O$_3$. The latter is crucial to carry out an accurate analysis for the electrochemical behaviours of the γ-Fe$_2$O$_3$/α-Fe$_2$O$_3$ powders in Li- and Na half cells, which are separately discussed in the next section.

Fig. 1 shows a group of micrographs, spectra and diffraction patterns related to the pyrolysed powders after air exposure. The black colour in all the images, spectra and diffraction patterns refers
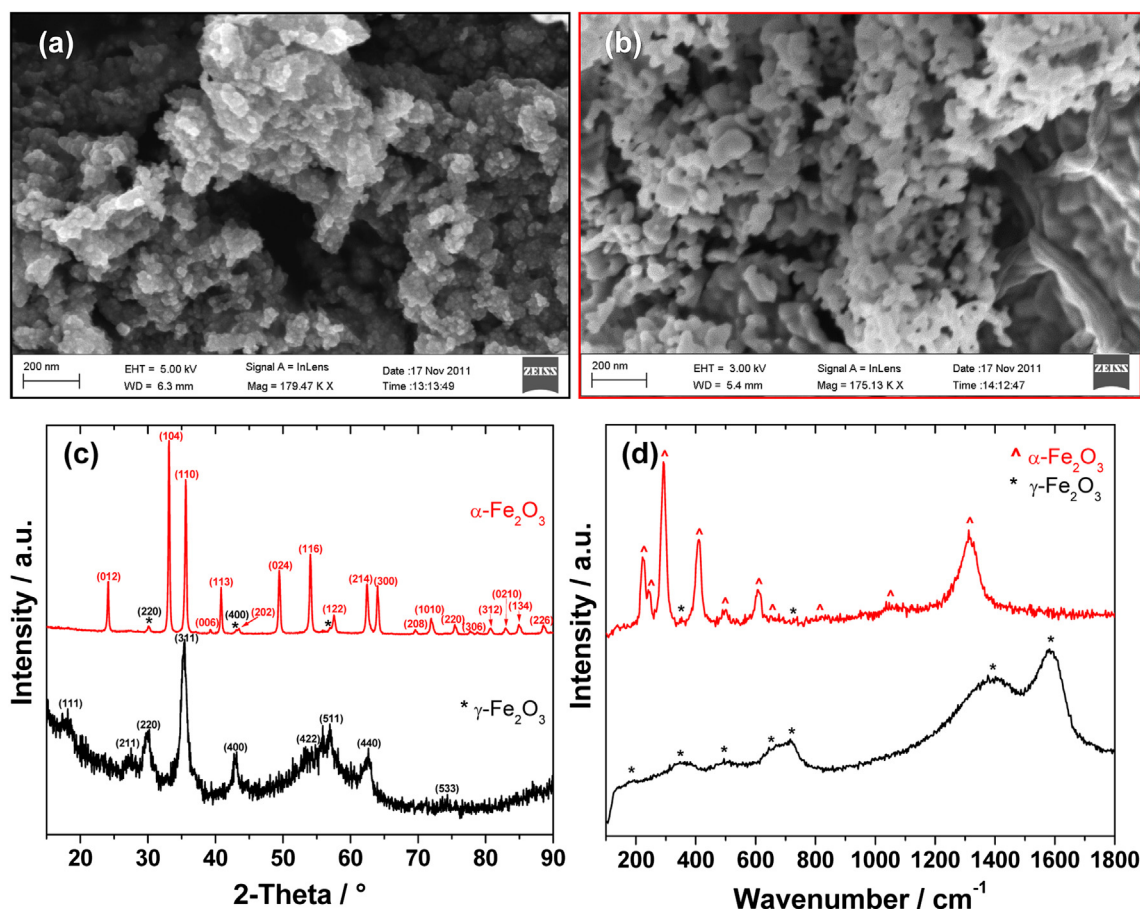
Fig. 1. SEM images (a, b) of the nanostructured powders synthesised via pyrolysis in vacuum at 260 °C after air exposure. (a) Morphology of the dark powders stable in air showing dense particle agglomeration. (b) Morphology of the red powders reacted in air exhibiting drop-like aggregates and prominent necking between the particles. (c) Normalised XRD patterns for the powders in (a) and (b). (d) Normalised Raman spectra for the powders shown in (a) and (b). All the diffraction patterns and spectra in black refer to the dark powders (i.e. γ-Fe$_2$O$_3$) stable in air, while those in red are related to the air-reacted material, which formed a bright red powder (i.e. α-Fe$_2$O$_3$). (For interpretation of the references to colour in this figure legend, the reader is referred to the web version of this article.)

to the powders stable in air (a), whereas the red one to those which underwent reaction upon air contact (b).

The respective SEM images show the different surface morphology for the resulting materials. The air-stable powders (Fig. 1a) displayed a dense particle agglomeration, with coexistence of agglomerates made of small nanoparticles and larger grainy structures. Vice versa, the reacted powders (Fig. 1b) exhibited mainly open nanostructured aggregates, where evident necking formed wider and elongated clusters.

The associated XRD patterns for both powders are presented in Fig. 1c. The diffractogram for the stable powders (see black curve) exhibited only few intense peaks and its overall pattern was typical of nanocrystalline materials, where amorphous parts contribute to the broad background. The diffraction pattern matched with that of a characteristic γ-Fe_2O_3 structure (JCPDF No. 39-1346), which here, however, could not be distinguished clearly from that of Fe_3O_4 (JCPDF No. 89-0691). The average crystallite size for γ-Fe_2O_3, calculated by the Scherrer's formula, yielded ≈ 18 nm, based on the (311) peak. By contrast, the diffraction pattern for the reacted powders (see red curve) was characterised by sharp peaks, which were unambiguously assigned to a α-Fe_2O_3 lattice structure (JCPDF No. 89-0596), though some traces of crystalline γ-Fe_2O_3 were detected in the diffractogram as well. The average crystallite size for the α-Fe_2O_3 phase from the Scherrer calculation was approximately 70 nm, based on the (104) peak, suggesting an increased degree of crystallinity after the reaction in air.

Micro-Raman analysis allowed complete discrimination of the various iron oxide phases obtained after air exposure. The spectrum associated with the air-stable powders (see black curve) was assigned to a pure maghemite phase [64,65]. Maghemite displays characteristic broad bands around 350, 500 and 700 cm^{-1}, which are sensitive to the degree of crystallinity of the material [66], as well as two prominent features around 1400 and 1600 cm^{-1}. Therefore, it was possible to distinguish the γ-Fe_2O_3 phase from that of a hypothetical Fe_3O_4 structure for the air-stable powders, since the respective Raman spectra are distinct [66]. The spectrum marked in red clearly indicated that the reacted powders were composed mostly of hematite, as noticed from the distinctive phonon lines that matched those of crystalline α-Fe_2O_3. Two characteristic A_{1g} modes were detected around 225 and 498 cm^{-1}, as well as four resolved E_g modes at 247, 293, 412 and 613 cm^{-1}, respectively [66,67]. Besides, the intense peak around 1320 cm^{-1} corresponded to a typical two-magnon scattering process, characteristic for hematite [66]. Some slight bumps were further observed in the same spectrum, which closely resembled those of a pure, crystalline α-Fe_2O_3 phase, whereas some weaker features due to γ-Fe_2O_3 were also detected (see the black asterisks on the red curve in Fig. 1d), in line with the XRD results.

TEM investigation enabled further insight into the structure, texture and crystallinity for the same powders after air exposure. Representative micrographs at different magnification are shown in Fig. 2 for the nanostructured γ-Fe_2O_3 and α-Fe_2O_3 powders.

The γ-Fe_2O_3 phase in Fig. 2a and b was constituted mainly of spherical-like nanoparticles displaying a dense agglomeration. The typical size of these particles spanned from roughly 8–20 nm, being most of them nano-crystals (i.e. grains made of a single crystallite) with distinctive lattice fringes. This matched well with the average crystallite size previously determined via Scherrer analysis. Some amorphous regions were also present in proximity of the grain boundaries in Fig. 2b. Interestingly, some large needle-like structures were detected together with the nanoparticle agglomerates. These needles had typical widths of about 250–400 nm, lengths of several microns and were surrounded by fluffy nanoparticle agglomerates (see inset of Fig. 2a). By contrast, the nanostructured α-Fe_2O_3 phase exhibited a different morphology,

structure and texture (Fig. 2c and d). The loose open structures in Fig. 2c displayed irregular shapes and were composed of elongated aggregates with evident necking between the adjacent particles, which resembled liquid droplets mutually connected via menisci. Spherical-like voids, ranging from few nanometers up to roughly 30 nm, were observed in these structures throughout the material. These pores were likely formed upon pyrolysis, due to the release of gaseous components, which left cavities into the reacting material. These aggregates appeared highly crystalline, as it is noticed from the sharp lattice fringes in Fig. 2d, showing that one of such elongated and mesoporous aggregates was indeed a single crystallite. Its crystalline domain extended for a length of about 80 nm. This matches well with the above Scherrer calculation for the average crystallite size of α-Fe_2O_3, though the crystallite shape was more ellipsoidal than spherical. Nevertheless, the HR-TEM analysis confirmed the increased degree of crystallinity in the reacted powders, probably due to local heating upon reaction and induced crystallisation, leading to grain growth and extensive necking.

The specific surface area of the final γ-Fe_2O_3/α-Fe_2O_3 mixture was studied by nitrogen adsorption-desorption tests and BET adsorption isotherms (see Supporting Information, Fig. S1) before the preparation of the electrode coatings. The calculated BET surface area was about 44 m^2 g^{-1}, while the cumulative volume of the pores by BJH calculation was approximately 0.1 cm^3 g^{-1}. The pore size distribution calculated from the desorption isotherm using the BJH analysis method indicated that a polydisperse ensemble of pores was present in the nanostructured powders, having an average width of about 12 nm.

The electrode coatings prepared with the nanostructured iron oxide powders, CMC binder and carbon additive were further investigated by SEM and EDS (see Supporting Information, Fig. S2) prior to their electrochemical analyses. The distribution of the various elements, which were separately imaged in different chemical maps, was homogeneous throughout the coated layer.

3.2. Electrochemical analysis

This section presents a detailed step-by-step comparison of the electrochemical properties for the coated electrodes tested in different Li- and Na half cells. The following sub-sections focus separately on cyclic voltammetry and galvanostatic tests, through which an exhaustive analysis of the associated reactions has been carried out.

3.2.1. Cyclic voltammetry

Preliminary electrochemical investigations of the nanostructured iron oxide-based electrodes were performed by CV on both Li- and Na half cells, as shown in Fig. 3, which compares the characteristic red-ox peaks upon respective uptake and removal of Li$^+$ ions (a) and Na$^+$ ions (b) at a scan rate of 0.1 mV s^{-1} between 0.05 and 3.0 V (i.e. *vs.* Li$^+$/Li or *vs.* Na$^+$/Na, depending on the cell type).

The first cathodic scan (i.e. Li$^+$ uptake) in Fig. 3a showed an initial inflection of the curve around 1.55 V, which was associated to the formation of a Li$_x$Fe$_2$O$_3$ compound [59,68]. The bump ('0') around 0.9 V was related to the early stage of iron oxide reduction and the associated structural changes preceding the generation of a solid electrolyte interface (SEI) layer. The latter usually takes place in this voltage region for TMOs cycled *vs.* lithium [53,68]. The SEI layer formation proceeded at lower voltages, as seen from the noticeable reduction peak ('I') around 0.5 V, which accompanied the conversion of Fe$_2$O$_3$ into Fe^0 and Li$_2$O [59,68]. Such a reaction changes irreversibly the structure, texture and crystallinity of the
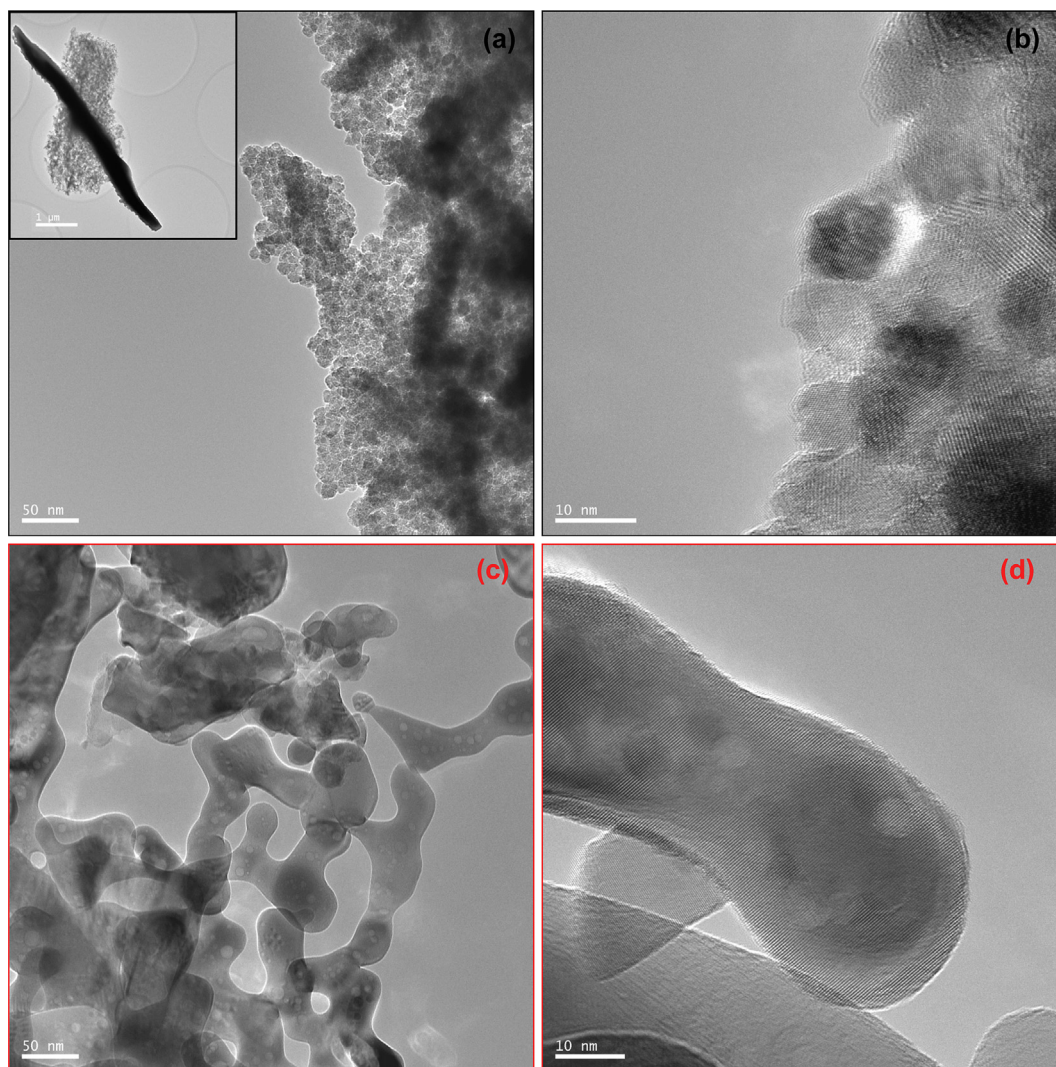
Fig. 2. TEM micrographs at different magnification of the nanostructured iron oxide powders obtained by pyrolysis in vacuum at 260 °C after air exposure. (a, b) Nanostructured γ-Fe$_2$O$_3$ phase stable upon air exposure. Note the dense agglomeration of crystalline nanoparticles in both (a) and (b). The inset in (a) shows the presence of long γ-Fe$_2$O$_3$ needles having larger size than the nanoparticle agglomerates. The scale bar in the inset is of 1 μm. (c, d) Nanostructured α-Fe$_2$O$_3$ phase deriving from the reaction of the pyrolysed powders with air. Note the open structure of the highly crystalline aggregates in (d) and the extended necking between adjacent structures. Voids or pores of different size are visible throughout the drop-like structures in both (c) and (d).

pristine material [69], as it implies the formation of new phase boundaries upon the nucleation of small (e.g. few nanometers) [53] iron nanoparticles in a surrounding matrix of amorphous Li$_2$O. The effects of such transformation were visible in the first anodic scan (i.e. Li$^+$ removal) in Fig. 3a, where the oxidation of the nano-sized Fe^0 particles proceeded in two-steps with a broad peak ('II') around 1.6 V and a shoulder ('II$_s$') at about 1.8 V. These two features correspond to a first oxidative reaction (i.e. Fe^0 → Fe^{+2}) and to further oxidation (i.e. Fe^{+2} → Fe^{+3}) [70], leading to a full regeneration of the iron oxide phase. The latter, however, was completely different from the pristine Fe$_2$O$_3$, since it resulted from the irreversible structural changes caused by the nucleation of the Fe^0 nanoparticles. In fact, such regenerated oxide is known to retain the interfaces created during its previous conversion and typically shows sizes comparable to those of the reduced metal nanoparticles [71]. Clear asymmetries between the reductive/oxidative processes upon Li$^+$ incorporation/release were also visible in Fig. 3a.

Quantification of the shifts in potential for the associated red-ox stages required some calculations (see Supporting Information) on

the basis of the neat electrochemical reaction occurring in the Li-half cell:

$$Fe_2O_3 + 6Li \leftrightarrow 2Fe + 3Li_2O \tag{2}$$

which should also cause a theoretical volume variation close to 93% for the iron oxide host and its conversion products. The standard potential (i.e. $E = E^0 = 1.626$ V vs. Li$^+$/Li), calculated on the basis of simplified thermodynamic assumptions, was, however, not far from the average value (i.e. ≈1.7 V vs. Li$^+$/Li) extracted from the oxidation peaks 'II' and 'II$_s$' in the first cycle of Fig. 3a. A slight overvoltage was thus present upon charge during Li$^+$ release. Conversely, the significant shift in the reduction potential for the main peak ('I') from the calculated value indicates that major changes occurred in the energy of the system upon initial conversion of the nanostructured Fe$_2$O$_3$ and SEI layer formation. In fact, if such shift would be caused by a mere polarization loss on discharge, e.g., due to the internal resistance of the cell, it should account for a discrepancy roughly comparable to that associated
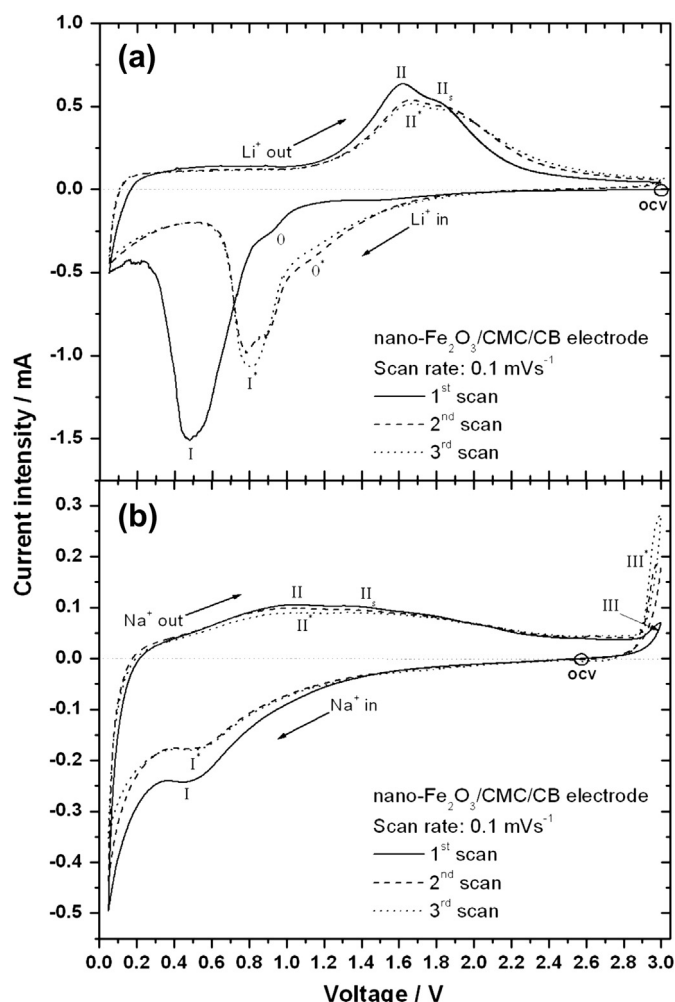
Fig. 3. CV plots for the composite electrode coatings with nanostructured Fe_2O_3 cycled in different half cells at a scan rate of 0.1 mV s^{-1}. (a) Li half cell cycled between 0.05 and 3.0 V *vs.* Li$^+$/Li. (b) Na half cell cycled between 0.05 and 3.0 V *vs.* Na$^+$/Na. The various stages of Li$^+$ and Na$^+$ uptake/removal in correspondence of the characteristic reduction/oxidation peaks are indicated. Asterisks refer to red-ox peaks after the first cycle.

with the overvoltage observed upon charge (e.g. 0.1–0.2 V), which was clearly not the case here. The noticeable shift of about 1.1 V between the thermodynamic value and the position of peak 'I' suggests that the nucleation of the Fe^0 nanoparticles involved a substantial energy expense for the system to generate new Fe^0/Li$_2$O phase boundaries, thus causing a further decrease in the cell voltage upon Li$^+$ incorporation.

On the one hand, the energy that the system has to spend to nucleate the highly-divided Fe^0 phase contributes to the large surface free energy excess of such nanoparticles, which are formed *in situ* and therefore are extremely reactive. On the other hand, the entire system gains also some energy, because it can incorporate more Li$^+$ ions than those allowed by an intercalation mechanism, increasing in this way the storage capacity of the electrode. The interfaces introduced in this process thus played a key role.

All the surface energies (i.e. surface tensions) were indeed changed, due to the creation of freshly-exposed interfaces for the iron nanoparticles (see Supporting Information). The crystallinity of the pristine oxide material was also important, because amorphization likely occurred upon conversion of the crystalline Fe$_2$O$_3$. The conversion mechanism further caused an electrochemical grinding [72,73] of the pristine particles, producing a size distribution for

both the Fe^0 and the regenerated Fe$_2$O$_3$ nanoparticles, which underwent red-ox reactions at different potentials, depending on their characteristic radius (see Supporting Information). This phenomenon could be inferred from the shape of both the cathodic and the anodic peaks in Fig. 3a. Their breadth indicated that the uptake and removal of Li$^+$ ions proceeded over a voltage range, due to the presence of a size distribution for both the nanostructured Fe$_2$O$_3$ and the Fe^0 nanoparticles. Besides, the asymmetry of the reactions was decreased in the second cycle, since the reduction peak 'I*' shifted to about 0.8 V *vs.* Li$^+$/Li, whereas the oxidation features 'II*' and 'II$_s$*' remained almost at the same positions. The initial voltage offset (i.e. ≈ -0.3 V) for the main peak 'I' in the first cycle can thus be ascribed to preliminary formatting and amorphization of the crystalline Fe$_2$O$_3$ upon conversion, accompanied by irreversible SEI formation. Nevertheless, the charge recovery at the end of the first cycle was rather good (i.e. $\approx 76\%$), as proven by the comparison between the areas subtended by the respective cathodic and anodic curves referred to the horizontal line (i.e., zero current). From the second and third cycle in Fig. 3a it is also seen that all the peak positions were maintained and that the shape of the curves almost coincided, indicating a good reversibility for the subsequent reactions.

Proceeding in an analogous way for the sodiation of Fe$_2$O$_3$, one would expect that the following reaction in a Na half cell could likewise take place:

$$Fe_2O_3 + 6Na \leftrightarrow 2Fe + 3Na_2O \tag{3}$$

Such electrochemical process would account for an overall theoretical volume change of about 215% and should yield a theoretical specific capacity of 1007 mAh g^{-1} on the basis of the molecular mass of Fe$_2$O$_3$ and the electrons/Na$^+$ ions exchanged in the process, similarly to Eq. (2). Nonetheless, the characteristic size, mass and mobility of Na$^+$ are certainly less favourable than those of Li$^+$ to yield such a completive reaction. An analogous calculation of the associated standard potential gives $E = E^0 = 0.664$ V *vs.* Na$^+$/Na (see Supporting Information).

The initial cathodic scan (i.e. uptake of Na$^+$ ions) in Fig. 3b did not exhibit any curve inflection from the OCV point and only a reductive peak ('I') was observed around 0.5 V *vs.* Na$^+$/Na. This feature should correspond to a conversion of the iron oxide accompanied by SEI formation, since the initial Na$^+$ insertion into Fe$_2$O$_3$ leads to the formation of a Na$_x$Fe$_2$O$_3$ (e.g. $0 < x < 2$) compound upon galvanostatic discharge to voltages around 1.2 V *vs.* Li$^+$/Li [51] (i.e., ≈ 0.9 V *vs.* Na$^+$/Na). A sloping tail was further noticed in Fig. 3b at lower voltages, where the cathodic current increased. A broad oxidation was seen upon subsequent Na$^+$ removal in the anodic part of the first cycle. Two weak bumps ('II' and 'II$_s$') were analogously detected around 1.0 and 1.4 V *vs.* Na$^+$/Na, corresponding to a two-step oxidation (i.e. Fe^0 → Fe^{+2} and Fe^{+2} → Fe^{+3}) that enabled iron oxide regeneration. A moderate increase of the anodic current occurred around 2.9 V ('III') and persisted up to 3.0 V. This oxidative feature is not completely clear, though it was presumably caused by some parasitic reaction, as it may be inferred from the following cycles, where the current intensity soared in correspondence of the same part ('III*') of the curves. A close comparison of the CV plots in Fig. 3 suggests that the conversion process upon sodiation/de-sodiation of Fe$_2$O$_3$ is not as pronounced as that occurring during its lithiation/de-lithiation, as well as the respective SEI-generating stages. The differences for the latter can be seen comparing the shape and the extension of the initial reductive peak for both processes. The reactions in the first sodiation/de-sodiation cycle were quite reversible (i.e. $\approx 72\%$ coulombic efficiency), as proved by the areas subtended by the respective cathodic and anodic curves referred to the horizontal

zero current line in Fig. 3b. Furthermore, the curve shape, apart from the oxidation at 2.9 V, was almost identical in the following cycles and no peak shifts were seen for the red-ox processes.

Fig. 4 compares the CV plots of the nanostructured Fe_2O_3 electrodes subsequently cycled vs. metal lithium (a) and metal sodium (b) at progressively increasing scan rates.

An overall enhancement of the peak current took place in both cases. The shape of the respective curves was preserved and, as the scan rate increased, it became more difficult to distinguish the oxidation peak from its shoulder, since they overlapped forming one extensive feature upon removal of both Li^+ and Na^+ ions. The distance in voltage between the red-ox couples (i.e. 'I*' and 'II*') as a function of the applied scan rate is also reported in Fig. 4 for the respective Li- (c) and Na (d) half cells. In Fig. 4c and d the trend of the data points extracted from the associated CV plots was clearly non-linear with the scan rate (see blue circles in web version), whereas the distance in voltage between the associated red-ox peaks varied in a linear way vs. the logarithm of the scan rate (see black squares). This would suggest that the limiting factor for such voltage discrepancy, ΔV_p, was not represented by an ohmic drop, but rather by major structural rearrangements in the material, which involved an activation step (e.g. nucleation). Interestingly, the initial distance in voltage between the red-ox peaks at the lowest scan rate for the Na-half cell was minor than that of the Li-half cell under the same conditions. Nevertheless, the slopes of the two lines in Fig. 4c and d were different and at higher scan rates the

value of ΔV_p increased proportionally more upon reaction with Na^+ than with Li^+. This is in agreement with the fact that these ions have different radii and atomic masses, which make the transfer of Na^+ less favourable than that of Li^+, especially in solid state reactions implying restructuring of the host material.
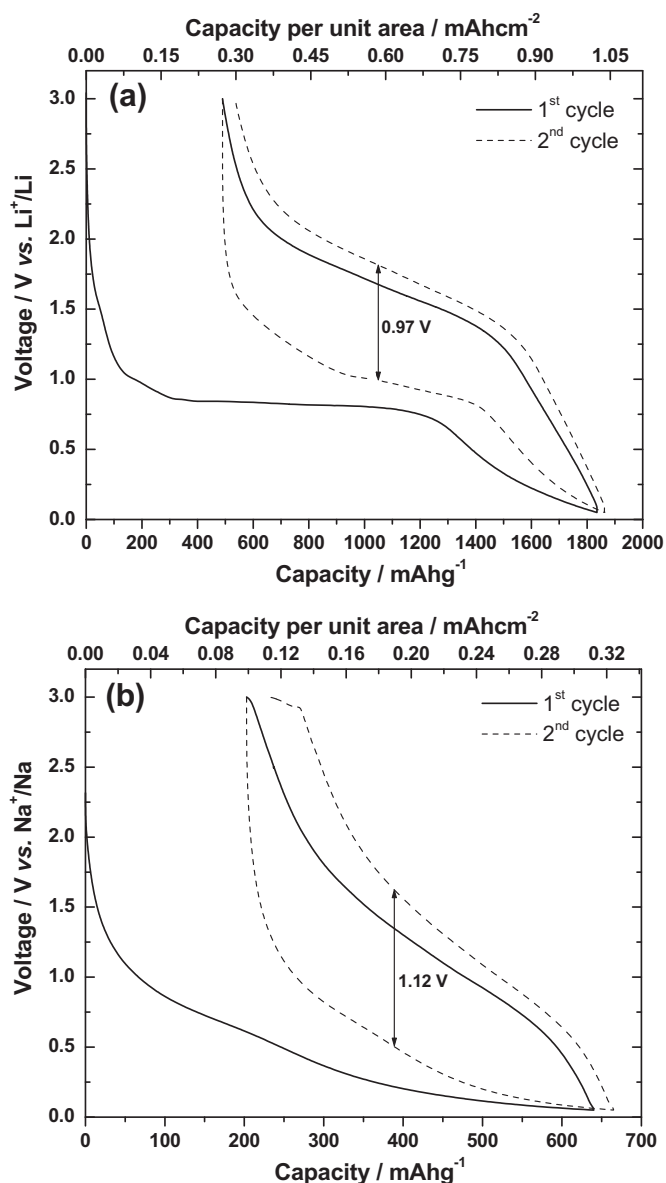
3.2.2. Galvanostatic tests

Fig. 5 presents the voltage profiles of the first two discharge/charge cycles for the nanostructured Fe_2O_3 electrodes tested under galvanostatic conditions in Li- (a) and Na half cells (b) applying a current density of about 130 and 40 mA g^{-1}, respectively.

The first discharge in Fig. 5a displayed all the characteristics features related to the various stages of lithiation of iron oxide and confirmed the previous CV results of Fig. 3a. The slight inflection of the discharge curve around 1.5 V corresponded to the initial formation of a $Li_xFe_2O_3$ compound [68], whereas the change in the slope around 1.0 V was related to the early stage of Fe_2O_3 reduction and the associated structural changes of the crystalline material upon impending conversion. The sharp plateau around 0.8 V was attributed to the irreversible formation of an SEI layer upon conversion of Fe_2O_3 into Fe^0 and Li_2O. The last part of the discharge exhibited a tail, corresponding to a pseudo-capacitive behaviour, which has been explained either in terms of interfacial storage [74–78] of Li^+ and e^- at the metal/Li_2O boundaries or of electrolyte decomposition and generation of a gel-like film catalysed by the metal nanoparticles [73,79,80]. The first discharge capacity,
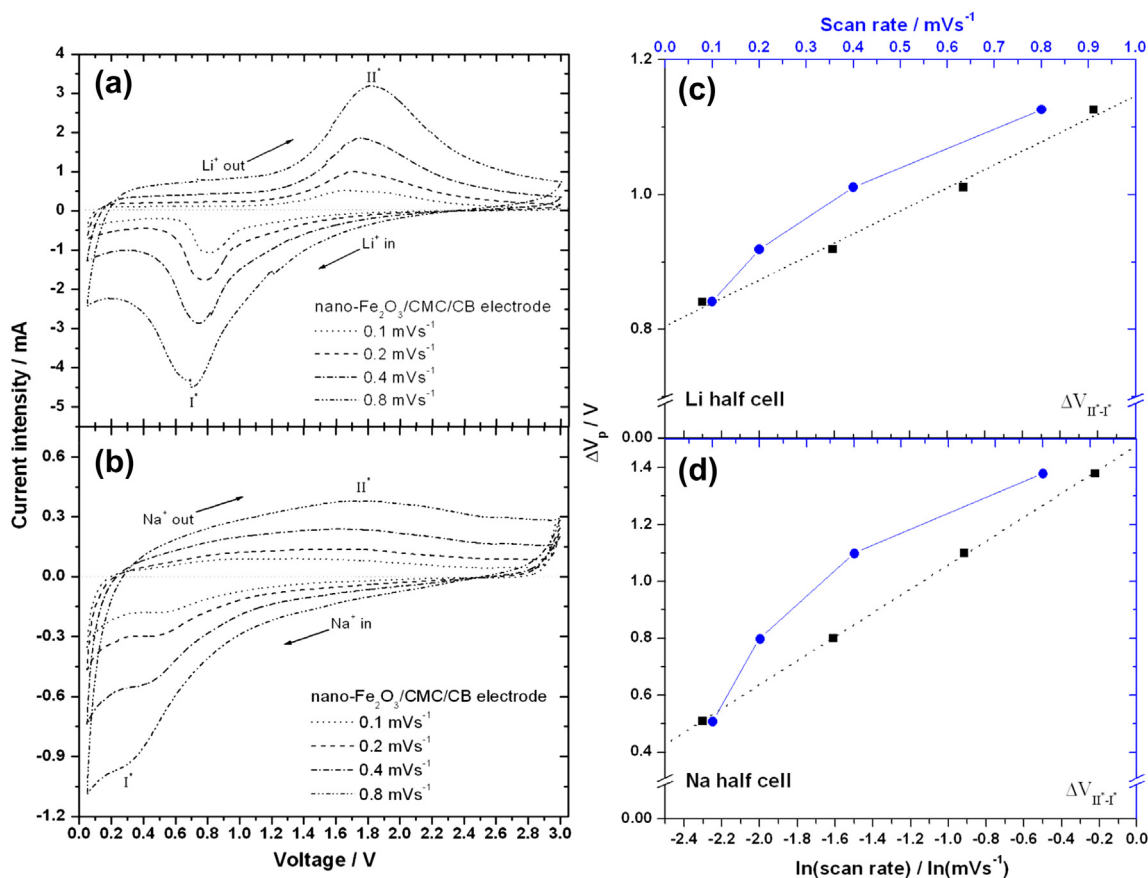
Fig. 4. CV plots for the composite electrode coatings with nanostructured Fe_2O_3 cycled in different half cells (a, b) at progressively increasing scan rates from 0.1 to 0.8 mV s^{-1}. (a) Li half cell cycled between 0.05 and 3.0 V vs. Li^+/Li at various rates. (b) Na half cell cycled between 0.05 and 3.0 V vs. Na^+/Na at increasing scan rates. Asterisks refer to red-ox peaks after the first cycle in (a, b). Comparison of the characteristic distance in voltage for the red-ox peaks extracted from the previous CV plots vs. the logarithm of the applied scan rate for: (c) Li half and (d) Na half cells. Note in both graphs the linear trend of the associated data points (black squares) and the non-linear behaviour for the coloured circles, which correspond to the applied scan rates.

Fig. 5. Voltage profile curves of the first two cycles of galvanostatic discharge/charge for the nanostructured Fe_2O_3 tested in different half cells. (a) Li half cell cycled with a 1 M $LiPF_6$ electrolyte between 0.05 and 3.0 V vs. Li^+/Li at a gravimetric current density of 130 mA g^{-1}. (b) Na half cell cycled with a 1 M $NaClO_4$ electrolyte between 0.05 and 3.0 V vs. Na^+/Na at a gravimetric current density of 40 mA g^{-1}.

referred to the active mass of Fe_2O_3 in the coating, was as high as 1835 mAh g^{-1} and yielded a capacity per unit area of about 1.01 mAh cm^{-2}. The first charge showed the characteristic asymmetries discussed above, e.g., a linear increase of the voltage up to 1.2 V, followed by a sloping plateau leading to the oxide regeneration. The capacity at the end of the first charge was approximately 73% of the initial discharge. However, a large discrepancy existed between the associated voltage profiles. This situation improved to a certain extent in the second cycle, due to some changes in the discharge curve, which exhibited a shift of the conversion plateau towards a higher voltage (see also Fig. 3a), as well as a more sloping profile. These characteristics were retained during the following discharges, confirming that the initial conversion of the pristine oxide irreversibly changed the properties of the host.

The second charge in Fig. 5a maintained all the previous features and displayed a separation in voltage of roughly 0.97 V between the

characteristic red-ox plateaus. Nonetheless, this figure alone could be misleading [57], since the most important quantity to consider is the *overall energy density* in the lozenge-shaped region (i.e., the overall area comprised between the ends of the discharge/charge curves), which provides a fair and general way to compare the energy efficiencies of various conversion materials, as well as those of any electrode. From the integrated areas subtended to the curves of the second discharge and charge, it was found that they had energy densities of 932.4 and 2128.0 Wh kg^{-1}, respectively. Their difference was the surplus of energy density required by the electrode system (i.e., from the external power source) to reverse the conversion reaction by rising its potential up to 3.0 V. This loss amounted to 56.2%, limiting the energy efficiency of the second cycle to 43.8%. The efficiency between the first charge and the second discharge in Fig. 5a was about 45.9%, accounting for a 54.1% loss between these subsequent half-cycles. Accordingly, the conversion step and the associated Fe^0 nucleation represented major energy expenses for the system, even after the first cycle.

Fig. 5b shows that the analogous processes of Na^+ uptake/ release were not comparable with those of Li^+, even at a lower current density. The initial specific discharge capacity was 640 mAh g^{-1}, corresponding to a capacity per unit area of about 0.31 mAh cm^{-2}. The discharge profile did not exhibit any sharp plateau, but rather a bump around 0.6 V, followed by a long tail at lower voltage, which contributed to almost half of the initial capacity. Therefore, a noticeable difference for the SEI formation and conversion processes existed for the lithiation and sodiation of iron oxide, matching with the above results. The specific capacity due to Fe_2O_3 sodiation was much lower than that predicted from Eq. (3), reinforcing the idea that a full conversion could not occur in this case. The severe volume change related to Eq. (3) should also affect the cycling properties of the electrode and likely cause a marked capacity fading. Nevertheless, the capacity recovered in the first charge was $\approx 69.0\%$ of the initial value and only a moderate fading was noticed in the following cycles (see Figs. 5b and 6).

The features of the first charge curve upon de-sodiation were quite similar to those of de-lithiation, though some differences were observed in the various sloping parts of the respective profiles. The charge curve in Fig. 5b bent at a lower potential (e.g. ≈ 0.5 V vs. Na^+/Na) compared to that of Fig. 5a (e.g. ≈ 1.2 V vs. Li^+/Li). The sloping plateau due to Na^+ release and Fe_2O_3 regeneration in Fig. 5b also had a higher slope. Similar considerations hold in Fig. 5b for the steeper part of the charge curve at higher voltage, which exhibited an anomalous inflection close to the cut-off point. This spurious feature (e.g. a parasitic reaction) was observed more clearly in the second charge around 2.9 V, confirming the previous results of Fig. 3b.

The first cycle had an energy efficiency of $\approx 51.3\%$, whereas the losses due to the voltage hysteresis (i.e. ≈ 1.12 V gap between the red-ox processes) in the second discharge/charge cycle were about 63.0%. Besides, the energy loss between the first half cycle of charge and the following half of discharge was roughly 59.7%.

The capacity retention for the same Li- and Na half cells is shown in Fig. 6, where the differences in the performance for these electrochemical systems are evident.

The reactions involving Li^+ ions clearly favoured both capacity and rate capability (i.e. applied current density), as it was noticed from the stable specific gravimetric capacity, which, after 30 cycles, was as high as 1400 mAh g^{-1} at 130 mA g^{-1}. This result, however, was not surprising, since stable cycling performances — though with lower capacities — have previously been obtained even for micrometer-sized α-Fe_2O_3 powders by an appropriate choice of the binder [81]. CMC ensured here a good cycling of the nanostructured iron oxide in both cells, where its improved adhesion to the Fe_2O_3 surface contributed to retain capacity [81] upon repeated volume
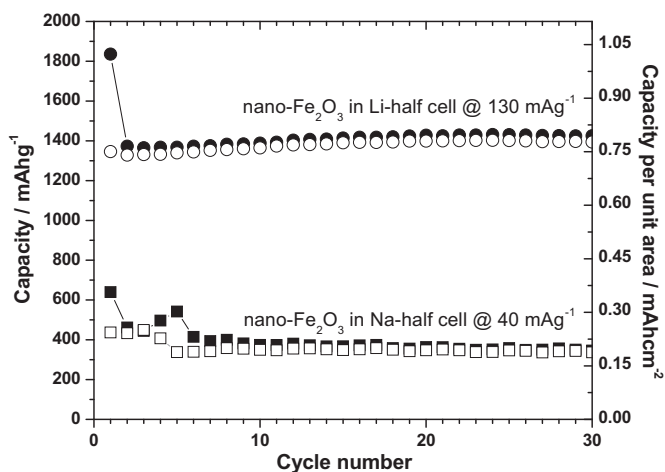
Fig. 6. Comparison of the cycle performances for the nanostructured Fe₂O₃ tested under galvanostatic conditions in distinct Li- and Na half cells using different current densities, as explained in Fig. 5.

changes undergone by the coated electrodes. CMC likewise favoured networking of the carbon additive [82] with the nanostructured Fe₂O₃ surface in the coating. This promoted the electrical conduction to and from the active structures, which is crucial, since the performances of α-Fe₂O₃ nanoparticles are very dependent on the carbon fraction in composite electrodes [83,84]. In this respect, it is worth mentioning that the performances of the present Fe₂O₃-based Li half cell were comparable, if not superior, to several morphology-engineered iron oxide composites having dedicated structures, such as: nanostructured reduced graphene oxide/Fe₂O₃ [85], hollow iron oxide nanoparticles [86] and spheres [87], hierarchical Fe₂O₃ microboxes [88], hollow-structured α-Fe₂O₃/C nanocomposites [89], hollow hematite nanosphere/carbon nanotube composites [90] and α-Fe₂O₃ hierarchical hollow spheres by a quasiemulsion templated method [91]. More importantly, the performances of the Na half cell in Fig. 6 demonstrate that it was possible to reversibly cycle this nanostructured Fe₂O₃ at 40 mA g⁻¹ between 0.05 and 3.0 V *vs.* Na⁺/Na with a conventional 1 M NaClO₄ electrolyte in EC:DEC without any additive. The specific capacity after 30 cycles was about 350 mAh g⁻¹, though a major fading occurred during the first six cycles. The latter could probably be ascribed to the spurious oxidation process at 2.9 V (see Figs. 3b and 5b).

Nonetheless, using a cut-off voltage of 2.8 V *vs.* Na⁺/Na prevented such detrimental feature, as it can be noticed from Fig. 7a. The correspondent discharge and charge profiles were obtained at a higher current density of 130 mA g⁻¹.

The voltage profiles were very similar to those of Fig. 5b, apart from the suppression of the anomalous oxidation upon charge. The lower capacity values observed in this case are due to the higher applied current. The initial capacity recovery was about 59%, while the energy efficiencies were respectively: 65.3% for the first discharge/charge, 39.6% for the second discharge/charge and 40.7% between the first charge and the second discharge. The associated cycle performances in Fig. 7b proved that, despite some fading, this nanostructured Fe₂O₃ could be cycled between 0.05 and 2.80 V even at 130 mA g⁻¹, providing ≈250 mAh g⁻¹ after 60 cycles. An earlier report on nanocrystalline α-Fe₂O₃ cycled with 1 M NaClO₄ in PC at 100 mA g⁻¹ between 1.2 and 4.0 V *vs.* Li⁺/Li showed, instead, a rapid capacity fading, retaining only ≈55 mAh g⁻¹ after 30 cycles [51]. Analogously, an electrodeposited thin film of Fe₂O₃ cycled with 1 M NaPF₆ (EC:DEC) between 0.05 and 3.0 V *vs.* Na⁺/Na at 5 μA cm⁻² completely lost its capacity in 8 cycles [92].
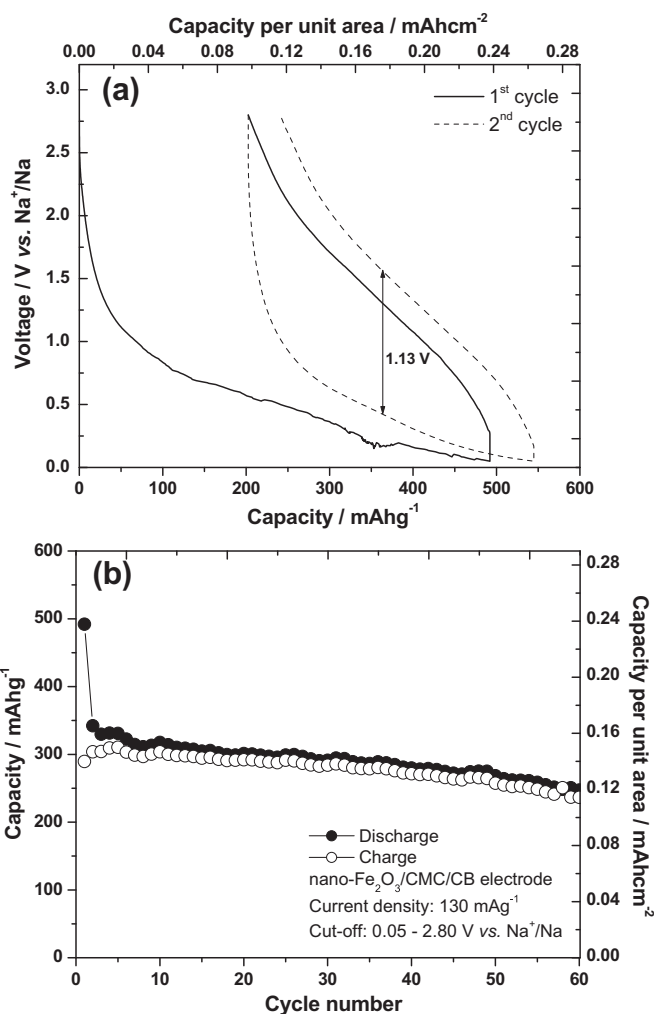
Fig. 7. Voltage profile curves of the first two galvanostatic cycles of discharge/charge for the nanostructured Fe₂O₃ cycled in a Na half cell between 0.05 and 2.80 V *vs.* Na⁺/Na at a gravimetric current density of 130 mA g⁻¹ (a). Cycle performance of the same electrode upon repeated cycles of discharge and charge (b).

As a final remark, it should be reminded that, despite the limitations brought about by replacing Li⁺ with Na⁺ ions, also a major benefit exists: unlike Li, Na does not electrochemically alloy with Al at low voltages, in line with Hume-Rothery rules [93]. This has a deep impact on the eventual fabrication of a Na-ion battery, since also the negative electrode could be coated on Al, instead of Cu, making the entire cell manufacture cheaper, more efficient and less polluting (see Table 1 in the Introduction). Substituting Cu with Al sensibly enhances the overall energy density of the cell, since Al is much lighter than Cu (i.e. 2.70 *vs.* 8.96 g cm⁻³) and this could eventually compensate for the other losses. The limited performances could be addressed by a dedicated cell and electrode design, while the cycling stability of such nanostructured Fe₂O₃ could further be improved by including additives in the electrolyte, as demonstrated for many other electrode systems.

4. Conclusions

Straightforward synthesis of nanostructured iron oxide at low temperature, as well as assembly into composite coatings including a cheap, water-soluble CMC binder have successfully been achieved. Overall, these preliminary results indicate that the

electrochemical sodiation of nanostructured Fe_2O_3 is reversible over an extended voltage range (e.g. 0.05–2.80 V vs. Na^+/Na). This could enable the use of such compound as a possible negative electrode in more sustainable preparations for novel, cost-effective Na-ion batteries, provided that its durability and cycle inefficiencies are conveniently addressed. Discharging iron oxide at low voltage vs. Na^+/Na offers a direct way to access higher storage capacities by a conversion mechanism similar to that occurring upon lithiation of Fe_2O_3, which has been analysed in parallel in this study.

Sodiation of Fe_2O_3 induced here a conversion which was not as pronounced as that caused by lithiation, as demonstrated by the previous electrochemical analyses. Evident performance limitations existed during uptake and removal of Na^+ in Fe_2O_3, as both its related specific capacities and applied current densities were not comparable with those achieved via Li^+ ions. This was likely due to the larger size of the Na^+ ions and their reduced mobility. Specific gravimetric capacities as high as 250 mAh g^{-1} were attained after 60 cycles at 130 mA g^{-1}, being this value still comparable with those of other state-of-the-art materials for Na-ion batteries. Nanostructured Fe_2O_3 yielded an average operational voltage of about 1.1 V vs. Na^+/Na under galvanostatic conditions, without displaying any sharp plateau, as differently observed during lithiation. Nevertheless, a clear voltage hysteresis in the discharge/charge profiles was present for both the reactions involving Na^+ and Li^+ ions, thus limiting the energy cycle efficiency and the overall energy density of the electrode. Although the asymmetries in the initial red-ox reactions of Fe_2O_3 were slightly less pronounced in the Na-based system, the surplus of energy required upon charge to regenerate the nanostructured Fe_2O_3 after its conversion was still significant. This likely suggests that the mobility of the various species involved in these reactions played an important role as well.

More efforts are finally needed to elucidate the surface interactions of such Fe_2O_3 with different Na-based electrolytes in order to improve the cycle performance of the electrodes by eventual use of additives.

Acknowledgements

Appendix A. Supplementary data

Supplementary data related to this article can be found at http://dx.doi.org/10.1016/j.jpowsour.2013.06.159.

References

[1] B.L. Ellis, W.R.M. Makahnouk, Y. Makimura, K. Toghill, L.F. Nazar, Nature Materials 6 (2007) 749–753.
[2] C. Wadia, P. Albertus, V. Srinivasan, Journal of Power Sources 196 (2011) 1593–1598.
[3] J.M. Tarascon, Philosophical Transactions of the Royal Society A: Mathematical, Physical and Engineering Sciences 368 (2010) 3227–3241.
[4] S.P. Ong, V.L. Chevrier, G. Hautier, A. Jain, C. Moore, S. Kim, X. Ma, G. Ceder, Energy and Environmental Science 4 (2011) 3680–3688.
[5] B.L. Ellis, L.F. Nazar, Current Opinion in Solid State and Materials Science 16 (2012) 168–177.
[6] M. D'Arienzo, R. Ruffo, R. Scotti, F. Morazzoni, C.M. Mari, S. Polizzi, Physical Chemistry Chemical Physics 14 (2012) 5945–5952.
[7] C. Delmas, J.J. Braconnier, C. Fouassier, P. Hagenmuller, Solid State Ionics 3–4 (1981) 165–169.
[8] E. Hosono, T. Saito, J. Hoshino, M. Okubo, Y. Saito, D. Nishio-Hamane, T. Kudo, H. Zhou, Journal of Power Sources 217 (2012) 43–46.
[9] Z. Lu, J.R. Dahn, Journal of the Electrochemical Society 148 (2001) A237–A240.
[10] M.M. Doeff, T.J. Richardson, L. Kepley, Journal of the Electrochemical Society 143 (1996) 2507–2516.
[11] F. Sauvage, L. Laffont, J.M. Tarascon, E. Baudrin, Inorganic Chemistry 46 (2007) 3289–3294.
[12] N. Yabuuchi, M. Yano, S. Kuze, S. Komaba, Electrochimica Acta 82 (2012) 296–301.
[13] M. Sathiya, K. Hemalatha, K. Ramesha, J.M. Tarascon, A.S. Prakash, Chemistry of Materials 24 (2012) 1846–1853.
[14] D. Kim, E. Lee, M. Slater, W. Lu, S. Rood, C.S. Johnson, Electrochemistry Communications 18 (2012) 66–69.
[15] S. Komaba, N. Yabuuchi, T. Nakayama, A. Ogata, T. Ishikawa, I. Nakai, Inorganic Chemistry 51 (2012) 6211–6220.
[16] S. Tepavcevic, H. Xiong, V.R. Stamenkovic, X. Zuo, M. Balasubramanian, V.B. Prakapenka, C.S. Johnson, T. Rajh, ACS Nano 6 (2012) 530–538.
[17] D. Hamani, M. Ati, J.M. Tarascon, P. Rozier, Electrochemistry Communications 13 (2011) 938–941.
[18] H. Liu, H. Zhou, L. Chen, Z. Tang, W. Yang, Journal of Power Sources 196 (2011) 814–819.
[19] S. Komaba, C. Takei, T. Nakayama, A. Ogata, N. Yabuuchi, Electrochemistry Communications 12 (2010) 355–358.
[20] S. Komaba, T. Nakayama, A. Ogata, T. Shimizu, C. Takei, S. Takada, A. Hokura, I. Nakai, ECS Transactions 16 (2009) 43–55.
[21] P. Moreau, D. Guyomard, J. Gaubicher, F. Boucher, Chemistry of Materials 22 (2010) 4126–4128.
[22] K. Zaghib, J. Trottier, P. Hovington, F. Brochu, A. Guerfi, A. Mauger, C.M. Julien, Journal of Power Sources 196 (2011) 9612–9617.
[23] K. Trad, D. Carlier, L. Croguennec, A. Wattiaux, M. Ben Amara, C. Delmas, Chemistry of Materials 22 (2010) 5554–5562.
[24] K. Trad, D. Carlier, L. Croguennec, A. Wattiaux, B. Lajmi, M. Ben Amara, C. Delmas, Journal of Physical Chemistry C 114 (2010) 10034–10044.
[25] K.T. Lee, T.N. Ramesh, F. Nan, G. Botton, L.F. Nazar, Chemistry of Materials 23 (2011) 3593–3600.
[26] R. Tripathi, G.R. Gardiner, M.S. Islam, L.F. Nazar, Chemistry of Materials 23 (2011) 2278–2284.
[27] Y. Kawabe, N. Yabuuchi, M. Kajiyama, N. Fukuhara, T. Inamasu, R. Okuyama, I. Nakai, S. Komaba, Electrochemistry 80 (2012) 80–84.
[28] B.L. Ellis, W.R. Michael Makahnouk, W.N. Rowan-Weetaluktuk, D.H. Ryan, L.F. Nazar, Chemistry of Materials 22 (2010) 1059–1070.
[29] B.L. Cushing, J.B. Goodenough, Journal of Solid State Chemistry 162 (2001) 176–181.
[30] Y. Lu, L. Wang, J. Cheng, J.B. Goodenough, Chemical Communications 48 (2012) 6544–6546.
[31] I.D. Gocheva, M. Nishijima, T. Doi, S. Okada, J.i. Yamaki, T. Nishida, Journal of Power Sources 187 (2009) 247–252.
[32] Y. Yamada, T. Doi, I. Tanaka, S. Okada, J.I. Yamaki, Journal of Power Sources 196 (2011) 4837–4841.
[33] P. Ge, M. Fouletier, Solid State Ionics 28–30 (1988) 1172–1175.
[34] D.A. Stevens, J.R. Dahn, Journal of the Electrochemical Society 148 (2001) A803–A811.
[35] D.A. Stevens, J.R. Dahn, Journal of the Electrochemical Society 147 (2000) 4428–4431.
[36] D.A. Stevens, J.R. Dahn, Journal of the Electrochemical Society 147 (2000) 1271–1273.
[37] S. Komaba, W. Murata, T. Ishikawa, N. Yabuuchi, T. Ozeki, T. Nakayama, A. Ogata, K. Gotoh, K. Fujiwara, Advanced Functional Materials 21 (2011) 3859–3867.
[38] R. Alcántara, J.M. Jiménez-Mateos, P. Lavela, J.L. Tirado, Electrochemistry Communications 3 (2001) 639–642.
[39] R. Alcántara, P. Lavela, G. Ortiz, J.L. Tirado, ECS Transactions 3 (2007) 191–198.
[40] R. Alcántara, P. Lavela, G.F. Ortiz, J.L. Tirado, Electrochemical and Solid-State Letters 8 (2005) A222–A225.
[41] Y. Cao, L. Xiao, M.L. Sushko, W. Wang, B. Schwenzer, J. Xiao, Z. Nie, L.V. Saraf, Z. Yang, J. Liu, Nano Letters 12 (2012) 3783–3787.
[42] V.L. Chevrier, G. Ceder, Journal of the Electrochemical Society 158 (2011) A1011–A1014.
[43] S. Komaba, Y. Matsuura, T. Ishikawa, N. Yabuuchi, W. Murata, S. Kuze, Electrochemistry Communications 21 (2012) 65–68.
[44] L. Baggetto, E. Allcorn, A. Manthiram, G.M. Veith, Electrochemistry Communications 27 (2013) 168–171.
[45] J. Qian, Y. Chen, L. Wu, Y. Cao, X. Ai, H. Yang, Chemical Communications 48 (2012) 7070–7072.
[46] L. Xiao, Y. Cao, J. Xiao, W. Wang, L. Kovarik, Z. Nie, J. Liu, Chemical Communications 48 (2012) 3321–3323.
[47] S. Komaba, T. Ishikawa, N. Yabuuchi, W. Murata, A. Ito, Y. Ohsawa, ACS Applied Materials and Interfaces 3 (2011) 4165–4168.
[48] M.N. Obrovac, L. Christensen, D.B. Le, J.R. Dahn, Journal of the Electrochemical Society 154 (2007) A849–A855.
[49] C. Didier, M. Guignard, C. Denage, O. Szajwaj, S. Ito, I. Saadoune, J. Darriet, C. Delmas, Electrochemical and Solid-State Letters 14 (2011) A75–A78.
[50] P. Senguttuvan, G. Rousse, V. Seznec, J.M. Tarascon, M.R. Palacín, Chemistry of Materials 23 (2011) 4109–4111.

[51] S. Komaba, T. Mikumo, N. Yabuuchi, A. Ogata, H. Yoshida, Y. Yamada, Journal of the Electrochemical Society 157 (2010) A60–A65.
[52] Y. Takeda, K. Nakahara, M. Nishijima, N. Imanishi, O. Yamamoto, M. Takano, R. Kanno, Materials Research Bulletin 29 (1994) 659–666.
[53] P. Poizot, S. Laruelle, S. Grugeon, L. Dupont, J.M. Tarascon, Nature 407 (2000) 496–499.
[54] N. Pereira, L. Dupont, J.M. Tarascon, L.C. Klein, G.G. Amatucci, Journal of the Electrochemical Society 150 (2003) A1273–A1280.
[55] H. Li, G. Richter, J. Maier, Advanced Materials 15 (2003) 736–739.
[56] X. Lou, X. Wu, Y. Zhang, Electrochemistry Communications 11 (2009) 1696–1699.
[57] P.G. Bruce, B. Scrosati, J.M. Tarascon, Angewandte Chemie International Edition 47 (2008) 2930–2946.
[58] M. Valvo, E. García-Tamayo, U. Lafont, E.M. Kelder, Journal of Power Sources 196 (2011) 10191–10200.
[59] M.M. Thackeray, W.I.F. David, J.B. Goodenough, Materials Research Bulletin 17 (1982) 785–793.
[60] F. Lévy, Intercalated Layered Materials, D. Reidel, Holland, 1979.
[61] F.M. Courtel, S. Niketic, D. Duguay, Y. Abu-Lebdeh, I.J. Davidson, Journal of Power Sources 196 (2011) 2128–2134.
[62] S.F. Lux, F. Schappacher, A. Balducci, S. Passerini, M. Winter, Journal of the Electrochemical Society 157 (2010) A320–A325.
[63] S. Musić, M. Ristić, S. Popović, Journal of Radioanalytical and Nuclear Chemistry 121 (1988) 61–71.
[64] T. Ohtsuka, K. Kubo, N. Sato, Corrosion 42 (1986) 476–481.
[65] N. Boucherit, A. Hugot-Le Goff, S. Joiret, Corrosion Science 32 (1991) 497–507.
[66] D.L.A. De Faria, S. Venâncio Silva, M.T. De Oliveira, Journal of Raman Spectroscopy 28 (1997) 873–878.
[67] I.R. Beattie, T.R. Gilson, Journal of the Chemical Society A: Inorganic, Physical, and Theoretical Chemistry (1970) 980–986.
[68] D. Larcher, C. Masquelier, D. Bonnin, Y. Chabre, V. Masson, J.B. Leriche, J.M. Tarascon, Journal of the Electrochemical Society 150 (2003) A133–A139.
[69] J. Cabana, L. Monconduit, D. Larcher, M.R. Palacín, Advanced Materials 22 (2010) E170–E192.
[70] J. Morales, L. Sánchez, F. Martín, F. Berry, X. Ren, Journal of the Electrochemical Society 152 (2005) A1748–A1754.
[71] M. Armand, J.M. Tarascon, Nature 451 (2008) 652–657.
[72] Y. Yu, Y. Shi, C.H. Chen, Nanotechnology 18 (2007) 055706.
[73] S. Grugeon, S. Laruelle, R. Herrera-Urbina, L. Dupont, P. Poizot, J.M. Tarascon, Journal of the Electrochemical Society 148 (2001) A285–A292.
[74] P. Balaya, H. Li, L. Kienle, J. Maier, Advanced Functional Materials 13 (2003) 621–625.
[75] J. Maier, Nature Materials 4 (2005) 805–815.
[76] P. Balaya, A.J. Bhattacharyya, J. Jamnik, Y.F. Zhukovskii, E.A. Kotomin, J. Maier, Journal of Power Sources 159 (2006) 171–178.
[77] J. Maier, Journal of Power Sources 174 (2007) 569–574.
[78] E. Bekaert, P. Balaya, S. Murugavel, J. Maier, M. Ménétrier, Chemistry of Materials 21 (2009) 856–861.
[79] S. Laruelle, S. Grugeon, P. Poizot, M. Dollé, L. Dupont, J.M. Tarascon, Journal of the Electrochemical Society 149 (2002) A627–A634.
[80] A. Ponrouch, P.L. Taberna, P. Simon, M.R. Palacín, Electrochimica Acta 61 (2012) 13–18.
[81] J. Li, H.M. Dahn, L.J. Krause, D.B. Le, J.R. Dahn, Journal of the Electrochemical Society 155 (2008) A812–A816.
[82] B. Lestriez, S. Bahri, I. Sandu, L. Roué, D. Guyomard, Electrochemistry Communications 9 (2007) 2801–2806.
[83] F. Jiao, J. Bao, P.G. Bruce, Electrochemical and Solid-State Letters 10 (2007) A264–A266.
[84] P.C. Wang, H.P. Ding, T. Bark, C.H. Chen, Electrochimica Acta 52 (2007) 6650–6655.
[85] X. Zhu, Y. Zhu, S. Murali, M.D. Stoller, R.S. Ruoff, ACS Nano 5 (2011) 3333–3338.
[86] B. Koo, H. Xiong, M.D. Slater, V.B. Prakapenka, M. Balasubramanian, P. Podsiadlo, C.S. Johnson, T. Rajh, E.V. Shevchenko, Nano Letters 12 (2012) 2429–2435.
[87] H.J. Kim, K.I. Choi, A. Pan, I.D. Kim, H.R. Kim, K.M. Kim, C.W. Na, G. Cao, J.H. Lee, Journal of Materials Chemistry 21 (2011) 6549–6555.
[88] L. Zhang, H.B. Wu, S. Madhavi, H.H. Hng, X.W. Lou, Journal of the American Chemical Society 134 (2012) 17388–17391.
[89] S.L. Chou, J.Z. Wang, D. Wexler, K. Konstantinov, C. Zhong, H.K. Liu, S.X. Dou, Journal of Materials Chemistry 20 (2010) 2092–2098.
[90] S.L. Chou, J.Z. Wang, Z.X. Chen, H.K. Liu, S.X. Dou, Nanotechnology 22 (2011) 265401.
[91] B. Wang, J.S. Chen, H.B. Wu, Z. Wang, X.W. Lou, Journal of the American Chemical Society 133 (2011) 17146–17148.
[92] M.C. López, P. Lavela, G.F. Ortiz, J.L. Tirado, Electrochemistry Communications 27 (2013) 152–155.
[93] W. Hume-Rothery, Journal of the Institute of Metals 35 (1926) 295–361.
[94] N.N. Greenwood, A. Earnshaw, Chemistry of the Elements, second ed., Elsevier, 1997.